


ORIGINAL ARTICLE

Open Access



# Potential of machine learning approaches for predicting mechanical properties of spruce wood in the transverse direction

Shuoye Chen<sup>1,2†</sup>, Rei Shiina<sup>1†</sup>, Kazushi Nakai<sup>3</sup>, Tatsuya Awano<sup>1</sup>, Arata Yoshinaga<sup>1</sup> and Junji Sugiyama<sup>1\*</sup> 

## Abstract

To predict the mechanical properties of wood in the transverse direction, this study used machine learning to extract the anatomical features of wood from cross-sectional stereograms. Specimens with different orientations of the ray parenchyma cell were prepared, and their modulus of elasticity (MOE) and modulus of rupture (MOR) were measured by a three-point bending test. The orientation of the ray parenchyma cell and wood density ( $\rho$ ) were used as parameters for the MOE and MOR prediction. Conventional machine learning algorithms and artificial neural network were used, and satisfactory results were obtained in both cases. A regular convolutional neural network (CNN) and a density-informed CNN were used to automatically extract anatomical features from the specimens' cross-sectional stereograms to predict the mechanical properties. The regular CNN achieved acceptable but relatively low accuracy in both the MOE and MOR prediction. The reason for this may be that  $\rho$  information could not be satisfactorily extracted from the images, because the images represented a limited region of the specimen. For the density-informed CNN, the average prediction coefficient for both the MOE and MOR drastically increased when  $\rho$  information was provided. A regression activation map was constructed to understand the representative anatomical features that are strongly related to the prediction of mechanical properties. For the regular CNN, the latewood region was highly activated in both the MOE and MOR prediction. It is believed that the ratio and orientation of latewood were successfully extracted for the prediction of the considered mechanical properties. For the density-informed CNN, the activated region is different. The earlywood region was activated in the MOE prediction, while the transition region between the earlywood and latewood was activated in the MOR prediction. These results may provide new insights into the relationship between the anatomical features and mechanical properties of wood.

**Keywords** Deep learning, Computer vision, Properties prediction, Structure–property relationships

## Introduction

Wood is an abundant and sustainable resource, and is widely used for construction, and in the manufacturing of, e.g., furniture, musical instruments, and paper. Because wood is a natural material, its properties vary owing to the unique anatomical features of different wood species, which are influenced by the growth environment [1]. Such variations are occasionally considered to be problematic because they deteriorate the utilization rate of wood resources. Therefore, understanding the relationship between the anatomical features and the mechanical properties is the subject of ongoing

<sup>†</sup>Shuoye Chen and Rei Shiina have contributed equally to this work.

\*Correspondence:

Junji Sugiyama  
sugiyama.junji.6m@kyoto-u.ac.jp

<sup>1</sup> Graduate School of Agriculture, Kyoto University, Kitashirakawa  
Oiwake-Cho, Sakyo-Ku, Kyoto 606-8502, Japan

<sup>2</sup> Research Institute for Sustainable Humanosphere, Kyoto University,  
Gokasho, Uji 611-0011, Japan

<sup>3</sup> Musical Instruments and Audio Production Unit, Yamaha Corporation,  
10-1, Nakazawa-Cho, Naka-Ku, Hamamatsu, Shizuoka 430-8650, Japan

investigation, and a system for the rapid evaluation of properties is urgently needed by the wood industry.

With the development of artificial intelligence (AI), machine learning has been effectively used as a powerful approach for the rapid prediction of the physical properties of materials, and can accelerate the speed of material design [2]. Additionally, machine learning has been used to predict the mechanical properties of wood and wooden products. A pioneering study by Mansfield et al. [3] used an artificial neural network (ANN) to predict the modulus of elasticity (MOE) and modulus of rupture (MOR) of wood. Subsequently, the density ( $\rho$ ), moisture content (MC), microfibril angle, and diffraction pattern coefficient of the variation of the azimuthal intensity profile of the wood specimens were measured. These parameters were fed into the ANN to build predictive models. Additionally, the ANN architecture was used to predict the mechanical properties of heat-treated wood and the bonding quality of plywood [4–9]. By using near-infrared spectroscopy combined with partial least squares regression, the MC,  $\rho$ , microfibril angles, and mechanical properties [10–13] of wood can be estimated with good accuracy.

Recently, computer vision-based anatomy has been proposed for the automated recognition of wood anatomical features from macroscopic images to micrographs [14–20]. The combination of computed features and machine learning algorithms helps in understanding the differences and relationships among different wood species [14–17]. By conducting clustering analysis on the features calculated for different species, the species specificities were successfully extracted [18, 19]. Recently, deep-learning-based approach such as convolutional neural network (CNN) has achieved excellent performance in both automatic feature extraction from input images using convolutional layers and classification tasks using fully connected layers [21]. Several studies have already applied the CNN architecture to wood

identification [20, 22]. However, few studies have directly used the CNN architecture to extract anatomical features from wood images with the objective of predicting the mechanical properties, even though CNN has been used to predict the properties of several materials [23, 24]. Furthermore, explainable AI technology, such as gradient-weighted class activation mapping (Grad-CAM), has also been established to further understand and validate models [25]. If this technique is used to analyze a model for predicting the mechanical properties of wood, it may assist the discovery of anatomical features that are strongly related to the predicted mechanical properties.

This study prepared Sitka spruce specimens with different orientations of the ray parenchyma cells (ORP), from 0° to 90° at intervals of 10°, and measured the MOE and MOR of the specimens by conducting a three-point bending test. The ORP and density were considered as the parameters, and input into conventional machine algorithms and an ANN to predict the MOE and MOR of the specimens in the transverse direction. Secondly, the cross-sectional stereograms of those specimens were used to build a CNN model to predict the mechanical properties of the specimens. Finally, a regression activation map was constructed to visualize important stereogram regions that are strongly related to the predicted mechanical properties of the wood specimens.

## Materials and methods

### Preparation of specimens

Sitka spruce (*Picea sitchensis*) was used in this study. Two spruce logs labeled as A and B were collected and then divided into quarters. For log A (Fig. 1a), the top-right quarter and left-bottom quarter were labeled as A1 and A2, respectively. For log B (Fig. 1b), two end-matched quarters were labeled as B1 and B2, respectively.

Quarter A1 was cut into strips with the dimensions of 100 mm (length)  $\times$  10 mm (longitudinal)  $\times$  3 mm (thickness) with consideration to the ORP. The alignment of

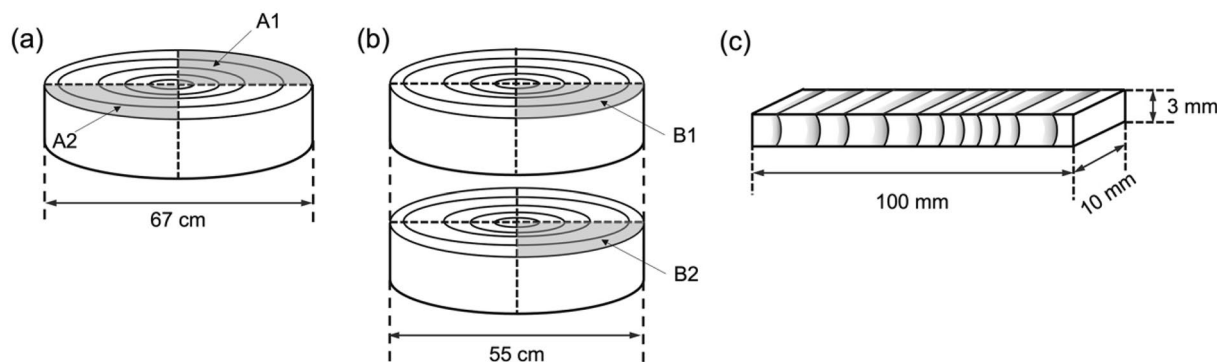


**Fig. 1** Logs cut into quarters and their selection for preparation of specimens: **a** log A; **b** log B; **c** prepared specimen with the ORP of 0°

the ray parenchyma cells in the horizontal and vertical direction was  $0^\circ$  and  $90^\circ$ , respectively. The specimens were prepared with the ORP in the range of  $0^\circ$ – $90^\circ$  at intervals of  $10^\circ$  through visual observation assisted by an angle scale. More than five specimens were prepared for each degree. The same process was also carried out for quarter A2, B1, and B2. Finally, 271 specimens were prepared.

Before observing the cross-section and conducting the three-point bending test, all specimens were conditioned at  $20^\circ\text{C}$  and 60% relative humidity (RH) for more than two weeks. The average  $\rho$  and MC of the specimens was  $0.48\text{ g/cm}^3$  and 11%, respectively.

#### Cross-sectional observation and three-point bending test

A sliding microtome (TU-213, Yamato Kohki industrial Co., Ltd., Japan) was used to smoothen the specimen's surface. Furthermore, the cell wall lumens were filled using chalk to increase the contrast of the cross-section. The images of the cross-section under bending spin were captured using a stereo-microscope (Leica DMS300, Leica Camera AG, Germany). The image size was  $1824\text{ pixels} \times 1168\text{ pixels}$  with RGB color, and the resolution was  $2.09\ \mu\text{m}$  per pixel. The central part of the captured images was cropped at the size of  $935\text{ pixels} \times 935\text{ pixels}$  and resized to  $256\text{ pixels} \times 256\text{ pixels}$  with 8 bit of gray scale with the resolution of  $7.64\ \mu\text{m}$  per pixel (Fig. 2). The preprocessed images were used for further analysis.

After microscopic observation, a three-point bending test was conducted using a universal testing machine (LSC 1/300-2, Tokyo testing machine, Japan) to measure

the MOE and MOR of the specimens. All experiments were conducted at  $20^\circ\text{C}$  and 60% RH. The test speed was set to  $10\text{ mm/min}$ , and the span of the specimens was  $65\text{ mm}$ .

#### Conventional machine learning algorithms and ANN for prediction of mechanical properties

As an important parameter indicating the orientation of wood cells, the precise ORP was calculated from the pre-processed images using the fast Fourier transform (FFT) method [15]. The obtained ORP and  $\rho$  were used as the input parameters to predict the MOE and MOR. Figure 3 shows the flowchart of the MOE and MOR prediction model.

The data were split using two methods, which will be described later. Subsequently, conventional machine learning approaches, namely, k-nearest neighbor (kNN), support vector machine (SVM), and random forest (RF), were used to build the corresponding models. For the kNN, the number of neighbors was set in the range of 1–10. The radial bias function kernel was used in the case of the SVM. The cost and gamma were considered as two hyperparameters, whose range is a logarithmic grid from  $10^0$  to  $10^5$  and  $10^{-1}$  to  $10^{-6}$ , respectively. For the RF, the number of estimators was set in the range of 100–1000 with 100 intervals.

An ANN was also used for prediction. Specifically, a multi-layer feed-forward network with backpropagation was used. The mean square error (MSE) was used as a loss function and Adam was used as the optimizer. This study used an ANN architecture with three hidden

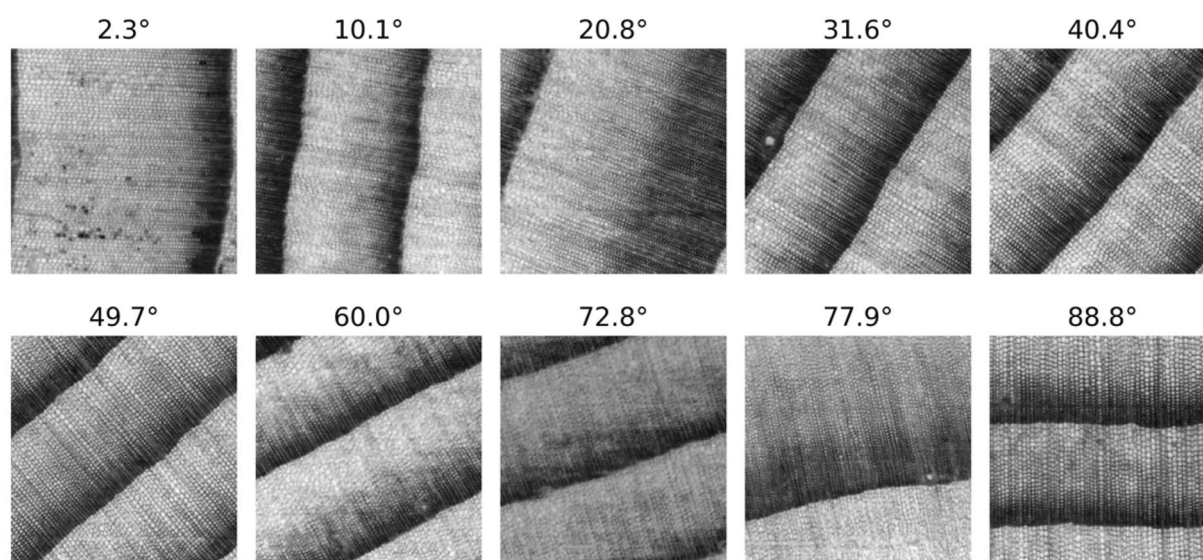


**Fig. 2** Typical cross-sectional images with different ORP. The numbers indicate the ORP degree of each specimen, which was calculated using the fast Fourier transform (FFT) method. Scale bar:  $800\ \mu\text{m}$

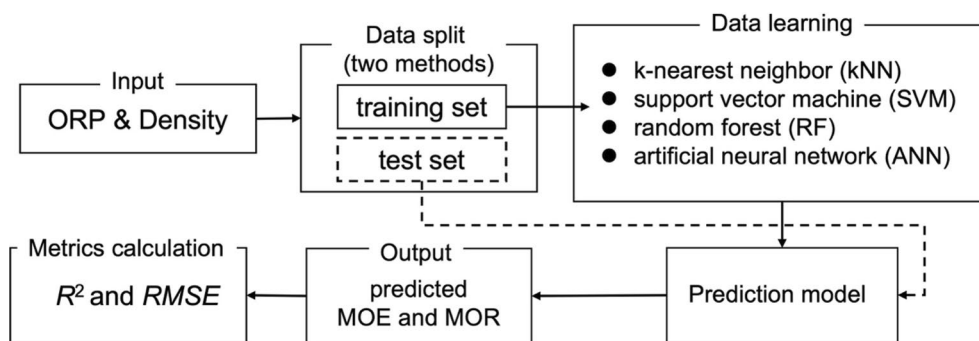


**Fig. 3** Flowchart of MOE and MOR prediction by conventional machine learning algorithms and ANN

layers. The number of neurons in each layer was set to 8, 16, or 32. The learning rate was set to 0.1, 0.01, 0.001, and 0.0001. The maximum number of training epochs was set to 1000. The optimal hyperparameters for the kNN, SVM, RF, and ANN were selected by performing grid search, respectively.

**Regular and density-informed CNN for prediction of properties**

This study also evaluated the potential of a CNN for MOE and MOR prediction based on the cross-sectional images of wood. Two CNN models were constructed in this study. The regular CNN contained six convolutional layers; a pooling layer was inserted every two convolutional layers, followed by three consecutive fully connected layers (Fig. 4). The number of filters for the three sets of convolutional layers was 16, 32, and 64, respectively. The size of the convolutional kernel was 5×5. In the pooling layers, the max pooling function and a kernel size of 4×4 were adopted. The number of neurons for each fully connected layer was 32. To accelerate the training, batch normalization was applied at the last fully connected layer. After each pooling layer and batch normalization, a dropout ratio of 0.3 was used to prevent overfitting. For the density-informed CNN, one neuron representing  $\rho$  was added to the first fully connected layer, and the rest of the structure was the same as that of a regular CNN. For both CNN

models, the rectified linear unit was used as the activation function, and the mean squared error was used as the loss function. The learning rate was set to 0.001, and Adam was used as the optimizer. The maximum number of training epochs was 1000. The model training was performed in Tensorflow 2.5.0.

**Data splitting method**

This study used two splitting methods to test the robustness of the trained model. The first method (Fig. 5a) used fourfold validation to select 25% of the data of each group; the remaining data were used as the training set. In the second method, one individual group was used as the test set, and the remaining groups were used as the training set (Fig. 5b).

**Model evaluation**

To evaluate the accuracy of the trained model, the coefficient of determination ( $R^2$ ) and root mean square error (RMSE) were used. The equations used to calculate  $R^2$  (Eq. 1) and  $RMSE$  (Eq. 2) are presented below:

$$R^2 = 1 - \frac{\sum_{i=1}^n (y_i - \hat{y}_i)^2}{\sum_{i=1}^n (y_i - \bar{y})^2}, \tag{1}$$

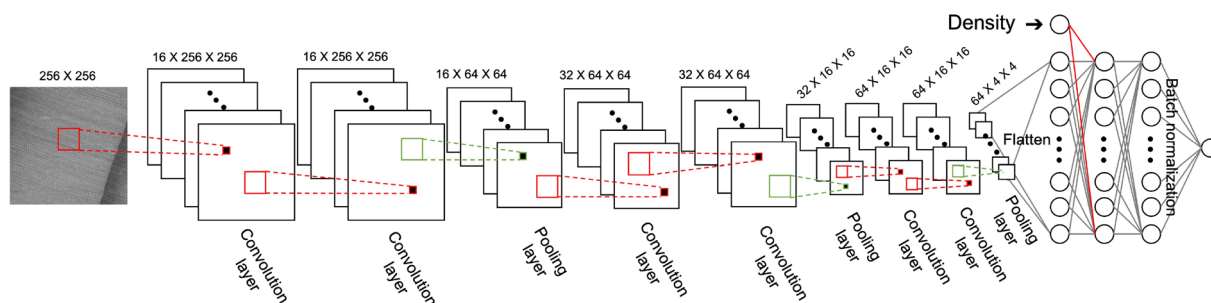


**Fig. 4** Architecture of density-informed CNN



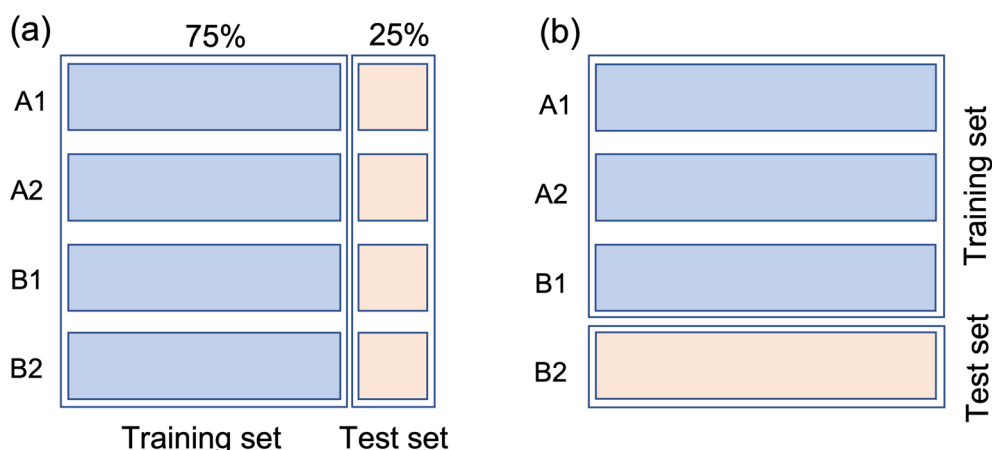


**Fig. 5** Method for splitting dataset: **a** splitting method #1; **b** splitting method #2

$$RMSE = \sqrt{\frac{1}{n} \sum_{i=1}^n (\hat{y}_i - y_i)^2}, \tag{2}$$

where  $n$  is the number of specimens in the dataset,  $y$  is the measured value,  $\hat{y}$  is the value predicted by the model, and  $\bar{y}$  is the mean value of  $y$ .

## Results and discussion

### Relationship between ORP and mechanical properties of wood in the transverse direction

Figure 6a, b shows the MOE and MOR of the specimens collected from logs A1, A2, B1, and B2 plotted against the ORP. A quadratic function was used to fit the trend of the MOE and MOR. Starting from 0°, both the MOE and MOR decreased as the ORP increased and reached a minimum value when the ORP was approximately 45°. These specimens were considered as rift-sawn specimens. Owing to the off-axis loading of the cells in a rift-sawn specimen, the shear deformation leads to the large flexural deformation of the wood. Hwang et al. [26] have confirmed this cell deformation for rift-sawn Japanese cedar (*Cryptomeria japonica*) and Japanese cypress (*Chamaecyparis obtusa*) specimens using the replica method. To analyze the cell deformation with time, Chen et al. [27] applied deep-learning-based semantic segmentation to partition individual wood cells, and quantitatively analyzed the evolution of cell shear deformation. They observed that both the MOE and MOR increased when the ORP was in the range of 45°–90°. The MOE and MOR of a 0° specimen, which is considered as a quarter-sawn specimen, are larger compared with those of a 90° specimen, which is considered as a flat-sawn specimen. The reason for this may be that the ray parenchyma cells in the quarter-sawn specimen are aligned in the horizontal direction of the bending test, which is parallel to the

tensile and compression direction, as has been discussed in a previous paper by the authors [27].

Because the A1 and A2 specimens were obtained from different parts of log A, as shown in Fig. 1a, their difference seems to be larger than that of the end-matched B1 and B2. As is known,  $\rho$  is strongly related to the mechanical properties of wood [28]. The averaged  $\rho$  with standard deviation of A1 and A2 are 0.41 (0.01) and 0.46 (0.02) g/cm<sup>3</sup>, respectively, while the averaged  $\rho$  with standard deviation of B1 and B2 were 0.54 (0.01) and 0.54 (0.04) g/cm<sup>3</sup>, respectively. Because tree growth is mainly stem enlargement, the  $\rho$  variation in the cross-section direction is larger than that in the vertical direction. The relationship between the ORP and the specific MOE, and that between the ORP and the specific MOR, were determined as shown in Fig. 6. By excluding the effect of  $\rho$ , the  $R^2$  of the polynomial fitting for the specific MOE and MOR is higher compared with that of the MOE and MOR. These results indicate that the ORP and  $\rho$  are important parameters influencing the mechanical properties of wood in the transverse direction.

### Potential of ORP and density as parameters for MOE and MOR prediction

As discussed above, the ORP and  $\rho$  are strongly related to the mechanical properties of wood in the transverse direction. Therefore, these two parameters were selected as the input parameters for the MOE and MOR prediction. Table 1 presents the accuracy of the MOE and MOR prediction by the conventional machine learning algorithms and ANN with the two data splitting methods. With splitting method #1, both the conventional machine learning approaches and the ANN achieved satisfactory performance. The  $R^2$  for both the MOE and MOR prediction was more than 0.8. Among

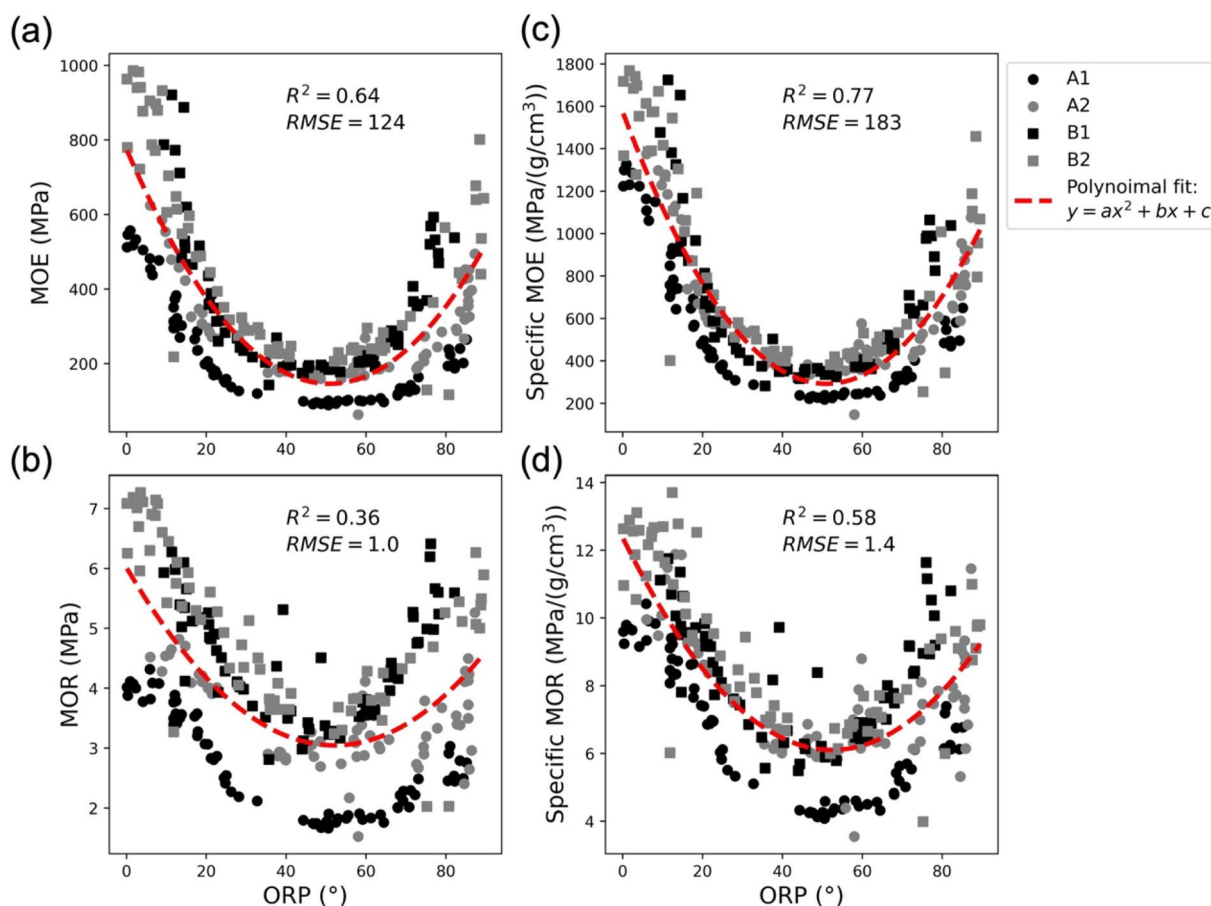


**Fig. 6** Relationship between ORP and mechanical properties of wood in the transverse direction. **a, b** MOE and MOR against ORP. **c, d** specific MOE and MOR divided by density against ORP

these approaches, the ANN achieved the best score on the test set with an  $R^2$  of 0.868 and RMSE of 72 MPa for the MOE prediction, while the kNN achieved the best score for the MOR prediction ( $R^2$  of 0.841 with RMSE of 0.51 MPa for the test set). The results also confirm that the ORP and  $\rho$  are important parameters influencing the mechanical properties of wood in the transverse direction.

In contrast, the accuracy deteriorated when splitting method #2 was used. Specifically, according to the metrics, the most inferior result was obtained when the A1 group was selected as the test set. Among the conventional machine learning approaches and the ANN, the SVM achieved relatively good prediction accuracy. As shown in Fig. 6, the mechanical properties of the specimens prepared from A1 are largely different compared with those of the specimens prepared from A2, B1, and B2. Therefore, the A1 test set may be outside of the applicability domain (AD) of the built model, which is the most likely reason for the low prediction accuracy.

Hence, to increase the AD of the established model, the number of specimens should be increased.

**Potential of CNN for ORP and density prediction**

The CNN is a well-established approach and has been extensively used in several computer vision tasks [20]. Additionally, the CNN has been used for the classification of wood species because it can achieve remarkable performance in the automatic extraction of anatomical features from images [22]. This study investigated the potential of CNN for predicting the mechanical properties of wood. First, the regular CNN was evaluated to confirm whether it is possible to extract ORP and  $\rho$  information. Table 2 presents detailed information regarding the accuracy of the ORP and density predictions.

For the ORP prediction, the CNN achieved excellent accuracy regardless of the splitting method, as shown in Fig. 7a. However, it was difficult for the CNN to recognize small density variations. Even when splitting method #1 was used, the average  $R^2$  of the test set was only approximately 0.357, which indicates that the density cannot be

**Table 1** Prediction accuracy of conventional machine learning approaches and ANN using two splitting methods

Learning algorithm	Splitting method	Group	MOE (MPa)		MOR (MPa)	
			$R^2$	RMSE	$R^2$	RMSE
KNN	Method #1	Train	0.879 (0.021)	71 (5)	0.870 (0.014)	0.47 (0.02)
		Test	0.839 (0.065)	80 (12)	0.846 (0.044)	0.50 (0.04)
	Method #2	Train <sub>A2,B1,B2</sub>	0.879	74	0.830	0.49
		Test <sub>A1</sub>	-0.657	176	-1.532	1.30
		Train <sub>A1,B1,B2</sub>	0.892	74	0.887	0.48
		Test <sub>A2</sub>	0.534	82	-0.347	0.84
		Train <sub>A1,A2,B2</sub>	0.902	66	0.891	0.45
		Test <sub>B1</sub>	0.847	72	0.617	0.57
		Train <sub>A1,A2,B1</sub>	0.893	52	0.872	0.39
		Test <sub>B2</sub>	0.701	141	0.498	0.92
SVM	Method #1	Train	0.870 (0.020)	74 (5)	0.857 (0.018)	0.49 (0.03)
		Test	0.855 (0.051)	77 (8)	0.843 (0.063)	0.51 (0.08)
	Method #2	Train <sub>A2,B1,B2</sub>	0.867	78	0.824	0.50
		Test <sub>A1</sub>	0.406	106	-0.430	0.98
		Train <sub>A1,B1,B2</sub>	0.879	78	0.877	0.50
		Test <sub>A2</sub>	0.710	65	0.028	0.71
		Train <sub>A1,A2,B2</sub>	0.888	71	0.871	0.49
		Test <sub>B1</sub>	0.763	89	0.635	0.55
		Train <sub>A1,A2,B1</sub>	0.816	68	0.869	0.40
		Test <sub>B2</sub>	0.703	141	0.555	0.86
RF	Method #1	Train	0.980 (0.003)	29 (1)	0.977 (0.003)	0.20 (0.01)
		Test	0.862 (0.033)	75 (7)	0.806 (0.039)	0.57 (0.06)
	Method #2	Train <sub>A2,B1,B2</sub>	0.979	31	0.971	0.20
		Test <sub>A1</sub>	0.268	117	-0.699	1.06
		Train <sub>A1,B1,B2</sub>	0.979	33	0.979	0.21
		Test <sub>A2</sub>	0.643	72	-0.113	0.76
		Train <sub>A1,A2,B2</sub>	0.985	26	0.980	0.19
		Test <sub>B1</sub>	0.537	125	0.089	0.87
		Train <sub>A1,A2,B1</sub>	0.986	19	0.980	0.16
		Test <sub>B2</sub>	0.743	131	0.541	0.88
ANN	Method #1	Train	0.889 (0.019)	68 (5)	0.863 (0.014)	0.48 (0.02)
		Test	0.868 (0.064)	72 (15)	0.841 (0.062)	0.51 (0.08)
	Method #2	Train <sub>A2,B1,B2</sub>	0.884	72	0.815	0.51
		Test <sub>A1</sub>	0.194	123	-0.404	0.97
		Train <sub>A1,B1,B2</sub>	0.882	77	0.850	0.55
		Test <sub>A2</sub>	0.476	87	0.284	0.61
		Train <sub>A1,A2,B2</sub>	0.890	71	0.836	0.55
		Test <sub>B1</sub>	0.761	90	0.150	0.84
		Train <sub>A1,A2,B1</sub>	0.842	63	0.805	0.48
		Test <sub>B2</sub>	0.786	120	0.638	0.78

$R^2$ : determination of coefficient; RMSE: root mean square error

The values in parentheses indicate the standard deviation

predicted satisfactorily (Fig. 7b). When splitting method #2 was used, invalid  $R^2$  values were calculated owing to the low prediction accuracy. The possible reason for this may be that the local image of the cross-section may not

represent the density of the entire specimen. Therefore, the CNN may have not been able to extract  $\rho$  information. To achieve accurate MOE and MOR predictions,  $\rho$  information should be added in the next step.

**Table 2** Accuracy of regular CNN in prediction of specimen’s ORP and  $\rho$

Splitting method for regular CNN	Group	ORP (°)		Density (g/cm <sup>3</sup> )	
		R <sup>2</sup>	RMSE	R <sup>2</sup>	RMSE
Method #1	Train	0.991 (0.004)	2.4 (0.6)	0.674 (0.102)	0.034 (0.005)
	Test	0.972 (0.008)	4.4 (0.4)	0.357 (0.061)	0.048 (0.003)
Method #2	Train <sub>A2,B1,B2</sub>	0.990	2.7	0.809	0.021
	Test <sub>A1</sub>	0.892	8.9	- 469.166	0.112
	Train <sub>A1,B1,B2</sub>	0.986	3.0	0.677	0.039
	Test <sub>A2</sub>	0.927	6.9	- 4.211	0.049
	Train <sub>A1,A2,B2</sub>	0.986	3.5	0.073	0.056
	Test <sub>B1</sub>	0.973	3.4	- 10.321	0.045
	Train <sub>A1,A2,B1</sub>	0.986	3.1	0.053	0.049
	Test <sub>B2</sub>	0.975	4.1	- 5.815	0.085

The values in parentheses indicate the standard deviation

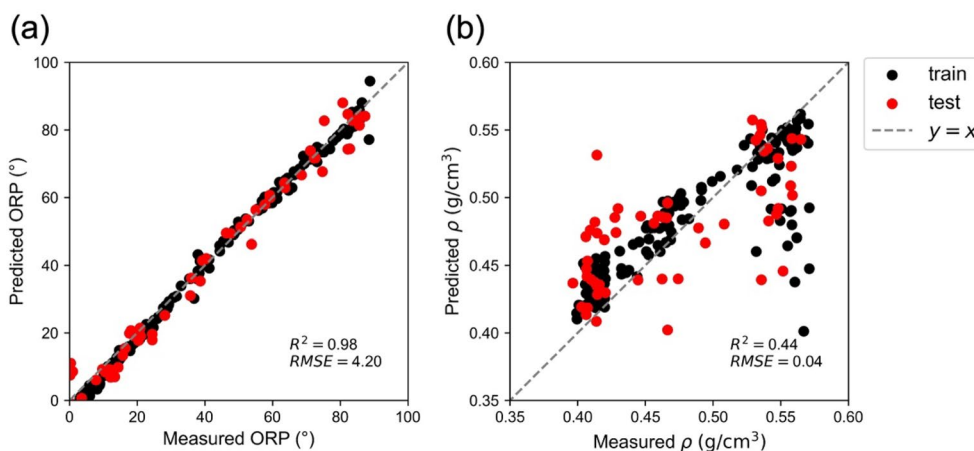


**Fig. 7** Accuracy of regular CNN in prediction of: **a** ORP and **b**  $\rho$  of specimen. The R<sup>2</sup> and RMSE were calculated from the test dataset

**Comparison of regular CNN and density-informed CNN for MOE and MOR prediction**

As described in the previous section, the regular CNN achieved excellent accuracy in the ORP prediction, but low accuracy in the  $\rho$  prediction. The MOE and MOR prediction may deteriorate without  $\rho$  information. To overcome this problem, a density-informed CNN was constructed by adding a neuron representing  $\rho$  to the first fully connected layer.

Table 3 compares the prediction accuracy of the regular CNN and density-informed CNN when using the two splitting methods. The regular CNN prediction has low but surprisingly acceptable accuracy. Even without  $\rho$  information, the average R<sup>2</sup> of the test set for the MOE and MOR using splitting method #1 was 0.735 and 0.536, respectively. It is possible that the CNN model did

not only extract the ORP information, but also extracted various additional anatomical features from the cross-sectional images to predict the mechanical properties. Some specimens with low MOE and MOR were not satisfactorily predicted, as shown in Fig. 8a, b. For the results of splitting method #2, similar to the results discussed in section of potential of ORP and density as parameters for MOE and MOR prediction, the accuracy drastically decreased, particularly when group A1 was used as the test set. Through the visual inspection of the cross-sectional images, it was found that averaged annual ring of specimens in A1 group (2.0 mm) was wider than that of the other groups (A2:1.5 mm; B1:1.0 mm; B2:1.3 mm), which possibly resulted in the low MOE and MOR of these specimens. In conclusion, the CNN model may not be able to clarify the relationship between anatomical



**Table 3** Accuracy of regular CNN and density-informed CNN in prediction of MOE and MOR of specimen

Learning algorithm	Splitting method	Group	MOE (MPa)		MOR (MPa)			
			$R^2$	RMSE	$R^2$	RMSE		
Regular CNN	Method #1	Train	0.929 (0.013)	56 (5)	0.855 (0.032)	0.50 (0.05)		
		Test	0.735 (0.048)	108 (14)	0.536 (0.076)	0.90 (0.11)		
	Method #2	Train <sub>A2,B1,B2</sub>	0.967	40	0.945	0.28		
		Test <sub>A1</sub>	-0.468	167	-3.50	1.74		
		Train <sub>A1,B1,B2</sub>	0.941	57	0.882	0.51		
		Test <sub>A2</sub>	0.125	113	-0.064	0.75		
		Train <sub>A1,A2,B2</sub>	0.914	62	0.862	0.50		
		Test <sub>B1</sub>	0.328	162	-0.880	1.14		
		Train <sub>A1,A2,B1</sub>	0.911	47	0.841	0.42		
		Test <sub>B2</sub>	0.200	238	-1.691	1.99		
		Density-informed CNN	Method #1	Train	0.961 (0.031)	39 (15)	0.953 (0.008)	0.29 (0.03)
				Test	0.859 (0.071)	77 (23)	0.812 (0.022)	0.54 (0.04)
Method #2	Train <sub>A2,B1,B2</sub>		0.947	50	0.972	0.20		
	Test <sub>A1</sub>		0.728	72	-0.249	0.92		
	Train <sub>A1,B1,B2</sub>		0.968	42	0.864	0.55		
	Test <sub>A2</sub>		0.646	72	0.255	0.63		
	Train <sub>A1,A2,B2</sub>		0.986	25	0.931	0.35		
	Test <sub>B1</sub>		0.771	94	0.572	0.55		
	Train <sub>A1,A2,B1</sub>		0.967	29	0.927	0.29		
	Test <sub>B2</sub>		0.651	155	0.423	0.92		

The values in parentheses indicate the standard deviation

features, such as the annual ring width, and mechanical properties when the model is trained on cross-sectional images from groups A2, B1, and B2.

However, when the specimen's  $\rho$  was given, the average  $R^2$  of the MOE drastically increased to 0.859 with an  $RMSE$  of 77 MPa, while the average  $R^2$  of the MOR increased to 0.812 with an  $RMSE$  of 0.54 MPa when using splitting method #1. Figure 8c, d shows the typical prediction results; the predictions for specimens with high MOE and MOR are not satisfactory. Interestingly, when using splitting method #2, the MOE predictions became more robust compared with the conventional machine learning approaches, ANN, and regular CNN. However, the  $R^2$  of MOR still showed a negative value when A1 group was selected as test set. In conclusion, combining features in the cross-sectional images and  $\rho$  information may provide more information for model training. However, because satisfactory accuracy was not achieved, a further increase in the number of specimens is needed. In this study, the collected cross-sectional images were two-dimensional and represented a limited area of the specimens. To further increase the accuracy, using three-dimensional images of wood obtained by high-resolution micro-computed tomography is considered as a promising method and should be investigated in future work.

### Regression activation map of regular CNN and density-informed CNN

After building the CNN models, the regression activation map was constructed to visually clarify important regions that the trained CNN should focus on to determine anatomical features that are strongly related to the predicted results. For both the regular CNN and the density-informed CNN, the fourth convolution layer was used for map construction. Figures 9 and 10 show the activation map for the MOE and MOR prediction, respectively. Notably, these activated regions were commonly observed regardless of the ORP of the specimens.

Figure 9a, b shows the activation maps of the regular CNN and density-informed CNN for the MOE prediction, respectively. The detailed procedure for the construction of activation maps is shown in Additional file 1: Fig. S1 and Additional file 1: Fig. S2. For the regular CNN, the activation region was concentrated in the entire latewood (LW) region (Fig. 9a). As is known, the annual ring consists of the earlywood (EW) region and LW region. The EW is formed at the beginning of the growing season, and has a thin cell wall and large cell lumen for water transportation. Compared with EW, the LW has a thicker cell wall and a small cell lumen, which results in higher density and plays an important role in the mechanical

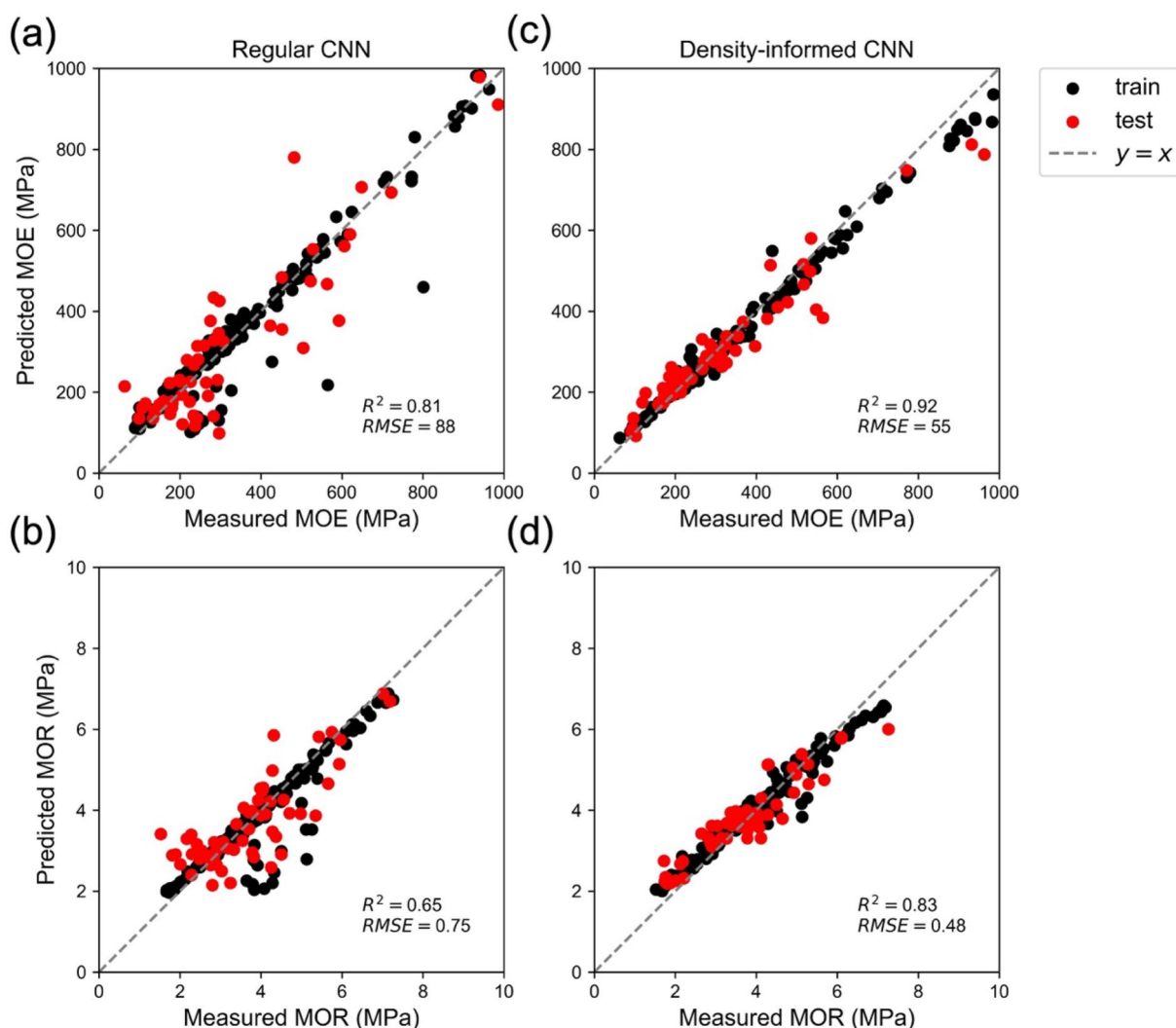


**Fig. 8** Accuracy of regular CNN and density-informed CNN in prediction of MOE and MOR of specimen. The  $R^2$  and  $RMSE$  were calculated from the test dataset. **a, b** MOE and MOR prediction by regular CNN; **c, d** MOE and MOR prediction by density-informed CNN

support of the tree [29]. Because the mechanical properties of LW are typically better than those of EW [30–32], the ratio of LW to EW is an important factor influencing the mechanical properties of wood. This study assumed that the ORP angle can be estimated by recognizing the LW region. Then, the annual ring width and LW amount can also be determined and used to obtain local  $\rho$  information from the observed image. By combining that information, it may be possible for the regular CNN to predict the MOE with acceptable accuracy (Table 3).

For the density-informed CNN, the  $\rho$  information was added to the first fully connected layer, and the activation region shifted from the LW region to the EW region (Fig. 9b). Because  $\rho$  information was provided, the LW ratio appears to be unimportant. Additionally, it

is possible that the CNN attempted to estimate a more accurate ORP angle by recognizing the LW region, because the EW region is typically larger than the LW region.

The activation regions of the MOR prediction are different to those of the MOE prediction (Fig. 10). For the regular CNN, the LW region was activated with an intensity gradient from the LW region to the transition region between EW and LW (Fig. 10a), because the MOR is defined as the final strength related to the failure of the specimen. In addition to the ORP and  $\rho$  information, anatomical features inducing specimen fracture should also be considered as another important factor influencing the MOR of the specimen. As discussed above, the mechanical properties of EW and LW are significantly

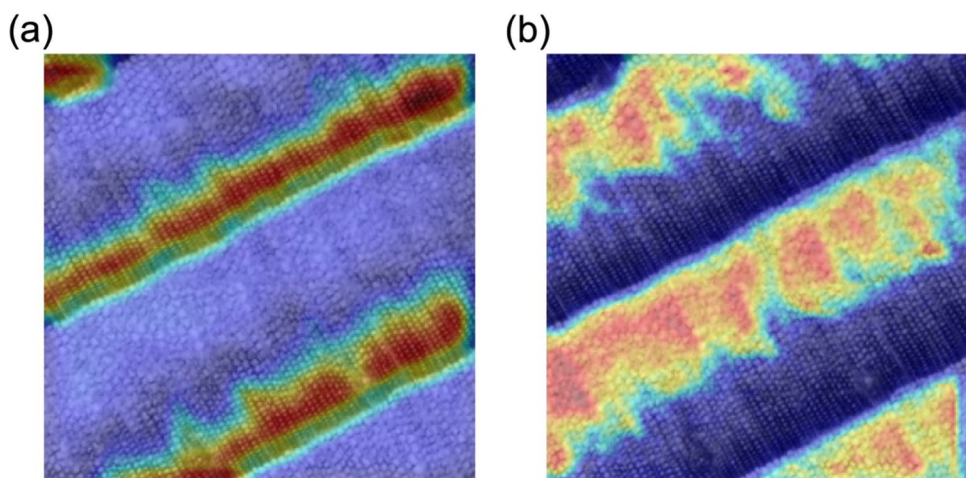


**Fig. 9** Activation maps of typical specimen for MOE prediction by **a** regular CNN and **b** density-informed CNN

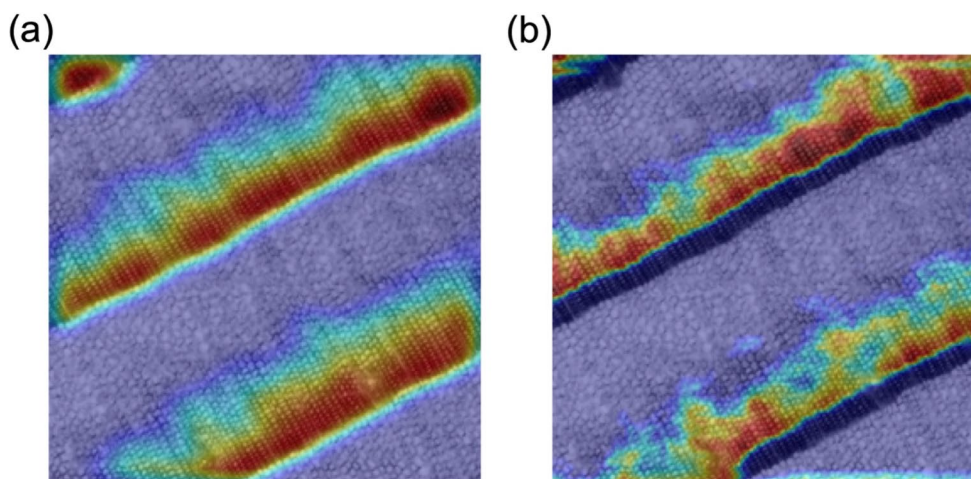


**Fig. 10** Activation maps of typical specimen for MOR prediction by: **a** regular CNN and **b** density-informed CNN

different. This contrast between EW and LW may be the reason for the specimen’s fracture during the mechanical test. Therefore, it is hypothesized that the regular CNN obtained the ORP and  $\rho$  information using the contrast between LW and EW, and thus realized the MOE prediction by recognizing the LW region.

Interestingly, for the density-informed CNN, the activated region shifted from the LW region to the transition region between EW and LW when  $\rho$  information was provided (Fig. 10b). When the local information of  $\rho$  is not required, it is possible that CNN shifts its attention to the precise recognition of the contrast between EW and LW. In addition to the proportion of EW and LW, whether the transition between them is gradual or

abrupt is another factor influencing the mechanical properties of wood [33]. It is hypothesized that the transition region between EW and LW provides a precise gradient of the changes in the mechanical properties. Moreover, it can also provide information about the ORP angle, which results in improved prediction accuracy for the density-informed CNN.

These results indicate that the regular CNN and density-informed CNN quantitatively recognized the anatomical features of wood in the cross-sectional images, and the activation map provides interesting information for understanding the relationship between the anatomical features and the mechanical properties of wood. Additionally, this suggests that machine learning

approaches have great potential for analyzing other anatomical features of wood. More precise analysis and further investigation should be conducted to confirm the importance of the anatomical features identified by machine learning approaches.

## Conclusions

This study used machine learning approaches to predict the mechanical properties of spruce wood in the transverse direction. A regular CNN and a density-informed CNN were built. The activation maps of both CNN models were constructed to understand the anatomical features that are strongly related to the prediction. The following conclusions were drawn from this study:

1. The ORP and density are recognized as two important parameters for predicting both the MOE and MOR of the specimens. By inputting these parameters into conventional machine learning algorithms and an ANN, a prediction model with good accuracy was successfully established.
2. A regular CNN and a density-informed CNN were successfully built to predict the mechanical properties of specimens based on corresponding cross-sectional stereograms. The density-informed CNN achieved better accuracy compared with the regular CNN, because it had an additional neuron that provided  $\rho$  information at the first fully connected layer.
3. The accuracy of the models built using conventional machine learning approaches, an ANN, a regular CNN, and a density-informed CNN was influenced by the data splitting method. When splitting method #2 was used, the accuracy always deteriorated, possibly because the test group was outside of the AD of the constructed model. To overcome this problem, the number of specimens should be increased.
4. The regression activation map constructed for the density-informed CNN established to predict the mechanical properties in the transverse direction is different to the regression activation map constructed for the regular CNN. When  $\rho$  information was provided, the activation region of the MOE shifted from the LW region to the EW region, and the activation region of the MOR shifted from LW to the transition region between the EW and LW region.

The results obtained by this study reveal that machine learning approaches have great potential for gaining new insights into the relationship between the anatomical features and the mechanical properties of wood. These approaches can also be used to investigate other anatomical feature-related mechanical behaviors of wood.

## Abbreviations

AI	Artificial intelligence
ANN	Artificial neural network
MOE	Modulus of elasticity
MOR	Modulus of rupture
MC	Moisture content
CNN	Convolutional neural network
Grad-CAM	Gradient-weighted class activation map
ORP	Orientation of ray parenchyma cells
RH	Relative humidity
FFT	Fast Fourier transform
kNN	K-nearest neighbor
SVM	Support vector machine
RF	Random forest
MSE	Mean square error
RMSE	Root mean square error
AD	Applicability domain
LW	Latewood
EW	Earlywood

## Supplementary Information

The online version contains supplementary material available at <https://doi.org/10.1186/s10086-023-02096-z>.

**Additional file 1: Fig. S1.** Combining the original image and the heat map to have the activation map for the prediction of MOE. The region with a lighter color was considered to be highly related to the predicted result. **Fig. S2.** Combining the original image and the heat map to have the activation map for the prediction of MOR. The region with a lighter color was considered to be highly related to the predicted result

## Acknowledgements

We express our sincere thanks to Mr. Akio Adachi for the preparation of spruce wood specimens.

## Author contributions

Data curation: Rei Shiina, Kazushi Nakai; investigation: Shuoye Chen, Rei Shiina, Kazushi Nakai, Junji Sugiyama; Methodology: Shuoye Chen, Junji Sugiyama; supervision: Junji Sugiyama; writing—original draft: Shuoye Chen; writing—review and editing: Junji Sugiyama, Kazushi Nakai, Arata Yoshinaga, Tatsuya Awano.

## Funding

This study was supported by Grants-in-Aid for Scientific Research on an Innovative Area (Grant Number 18H05485) and JSPS Postdoctoral Fellowships for Research in Japan (Grant Number 22F22085) from the Japan Society for the Promotion of Science.

## Availability of data and materials

The detailed information that supports the findings of this study is available from the corresponding author upon reasonable request. And the necessary codes in this study are available online at [https://github.com/pywood21/prop\\_pred\\_2023](https://github.com/pywood21/prop_pred_2023).

## Declarations

### Competing interests

The authors declare that they have no competing interests directly relevant to the content of this article.

Received: 24 March 2023 Accepted: 15 June 2023

Published online: 25 June 2023



## References

- Ross RJ (2010) Wood handbook—wood as an engineering material, U.S. Dept. of Agriculture, Forest Service, Forest Products Laboratory, WI. <https://doi.org/10.2737/FPL-GTR-190>
- Guo K, Yang Z, Yu CH, Buehler MJ (2021) Artificial intelligence and machine learning in design of mechanical materials. *Mater Horiz* 8:1153–1172. <https://doi.org/10.1039/D0MH01451F>
- Mansfield SD, Iliadis L, Avramidis S (2007) Neural networks prediction of bending strength and stiffness in western hemlock (*Tsuga heterophylla* Raf.) *Holzforchung* 61:707–716. <https://doi.org/10.1515/HF.2007.115>
- Esteban LG, Fernandez FG, DePalacios P (2011) Prediction of plywood bonding quality using an artificial neural network. *Holzforchung* 65:209–214. <https://doi.org/10.1515/hf.2011.003>
- Tiryaki S, Hamzecebi C (2014) Predicting modulus of rupture (MOR) and modulus of elasticity (MOE) of heat treated woods by artificial neural networks. *Measurement* 49:266–274. <https://doi.org/10.1016/j.measurement.2013.12.004>
- Tiryaki S, Aydin A (2014) An artificial neural network model for predicting compression strength of heat treated woods and comparison with a multiple linear regression model. *Constr Build Mater* 62:102–108. <https://doi.org/10.1016/j.conbuildmat.2014.03.041>
- Nasir V, Nourian S, Avramidis S, Cool J (2019) Prediction of physical and mechanical properties of thermally modified wood based on color change evaluated by means of 'group method of data handling' (GMDH) neural network. *Holzforchung* 73:381–392. <https://doi.org/10.1515/hf-2018-0146>
- Fathi H, Nasir V, Kazemirad S (2020) Prediction of the mechanical properties of wood using guided wave propagation and machine learning. *Constr Build Mater* 262: 120848. <https://doi.org/10.1016/j.conbuildmat.2020.120848>
- Haftkhani AR, Abdoli F, Sepehr A, Mohebbi B (2021) Regression and ANN models for predicting MOR and MOE of heat-treated fir wood. *J Build Eng* 42: 102788. <https://doi.org/10.1016/j.jobe.2021.102788>
- Thygesen LG and Lundqvist SO (2000) NIR measurement of moisture content in wood under unstable temperature conditions. Part 2. Handling temperature fluctuations. *J Near Infrared Spectrosc* 8: 191–199. <https://doi.org/10.1255/jnirs.278>
- Kothiyal V, Raturi A (2011) Estimating mechanical properties and specific gravity for five-year-old *Eucalyptus tereticornis* having broad moisture content range by NIR spectroscopy. *Holzforchung* 66:757–762. <https://doi.org/10.1515/hf.2011.055>
- Fujimoto T, Kobori H, Tsuchikawa S (2012) Prediction of wood density independently of moisture conditions using near infrared spectroscopy. *J Near Infrared Spectrosc* 20:353–359. <https://doi.org/10.1255/jnirs.994>
- Ma T, Inagaki T, Tsuchikawa S (2017) Calibration of SilviScan data of *Crytomeria japonica* wood concerning density and microfibril angles with NIR hyperspectral imaging with high spatial resolution. *Holzforchung* 71:341–347. <https://doi.org/10.1515/hf-2016-0153>
- Kobayashi K, Akada M, Torigoe T, Imazu S, Sugiyama J (2015) Automated recognition of wood used in traditional Japanese sculptures by texture analysis of their low-resolution computed tomography data. *J Wood Sci* 61:630–640. <https://doi.org/10.1007/s10086-015-1507-6>
- Kobayashi K, Hwang SW, Lee WH, Sugiyama J (2017) Texture analysis of stereograms of diffuse-porous hardwood: identification of wood species used in Tripitaka Koreana. *J Wood Sci* 63:322–330. <https://doi.org/10.1007/s10086-017-1625-4>
- Hwang SW, Kobayashi K, Zhai S, Sugiyama J (2018) Automated identification of Lauraceae by scale-invariant feature transform. *J Wood Sci* 64:69–77. <https://doi.org/10.1007/s10086-017-1680-x>
- Kobayashi K, Hwang SW, Okochi T, Lee WH, Sugiyama J (2019) Non-destructive method for wood identification using conventional X-ray computed tomography data. *J Cult Herit* 38:88–93. <https://doi.org/10.1016/j.culher.2019.02.001>
- Kobayashi K, Kegasa T, Hwang SW, Sugiyama J (2019) Anatomical features of Fagaceae wood statistically extracted by computer vision approaches: some relationships with evolution. *PLoS ONE* 14: e0220762. <https://doi.org/10.1371/journal.pone.0220762>
- Hwang SW, Kobayashi K, Sugiyama J (2020) Detection and visualization of encoded local features as anatomical predictors in cross-sectional images of Lauraceae. *J Wood Sci* 66:16. <https://doi.org/10.1186/s10086-020-01864-5>
- Hwang SW, Sugiyama J (2021) Computer vision-based wood identification and its expansion and contribution potentials in wood science: a review. *Plant Methods* 17:47. <https://doi.org/10.1186/s13007-021-00746-1>
- Krizhevsky A, Sutskever I, Hinton GE (2012) ImageNet classification with deep convolutional neural networks. *Adv Neural Inf Process Syst* 25:1097–1105
- He T, Lu Y, Jiao L, Zhang Y, Jiang X, Yin Y (2020) Developing deep learning models to automate rosewood tree species identification for CITES designation and implementation. *Holzforchung* 74:1123–1133. <https://doi.org/10.1515/hf-2020-0006>
- Wu J, Yin X, Xiao H (2018) Seeing permeability from images: fast prediction with convolutional neural networks. *Sci Bull* 63:1215–1222. <https://doi.org/10.1016/j.scib.2018.08.006>
- Sigaki HYD, Lenzi EK, Zola RS (2020) Learning physical properties of liquid crystals with deep convolutional neural networks. *Sci Rep* 10:7664. <https://doi.org/10.1038/s41598-020-63662-9>
- Selvaraju RR, Cogswell M, Das A, Vedantam R, Parikh D, Batra D (2020) Grad-CAM: visual explanations for deep networks via gradient-based localization. *Int J Comput Vis* 128:336–359. <https://doi.org/10.1007/s11263-019-01228-7>
- Hwang SW, Isoda H, Nakagawa T, Sugiyama J (2021) Flexural anisotropy of rift-sawn softwood boards induced by the end-grain orientation. *J Wood Sci* 67:14. <https://doi.org/10.1186/s10086-021-01946-y>
- Chen S, Awano T, Yoshinaga A, Sugiyama J (2022) Flexural behavior of wood in the transverse direction investigated using novel computer vision and machine learning approach. *Holzforchung* 76:875–885. <https://doi.org/10.1515/hf-2022-0096>
- Gibson LJ (2012) The hierarchical structure and mechanics of plant materials. *J R Soc Interface* 9:2749–2766. <https://doi.org/10.1098/rsif.2012.0341>
- Domec JC, Barbara LG (2002) How do water transport and water storage differ in coniferous earlywood and latewood? *J Exp Bot* 53:2369–2379. <https://doi.org/10.1093/jxb/erf100>
- Ohagama T, Yamada T (1981) Young's moduli of earlywood and latewood in transverse direction of softwoods. *Zairyo* 30:707–711. <https://doi.org/10.2472/jsms.30.707>
- Krauss A, Moliński W, Kúdela J, Cunderlík I (2011) Differences in the mechanical properties of early and latewood within individual annual rings in dominant pine tree (*Pinus sylvestris* L.) *Wood Res* 56: 1–12.
- Büyüksarı Ü, As N, Dündar T (2017) Mechanical properties of earlywood and latewood sections of scots pine wood. *Bioresources* 12:4004–4012. <https://doi.org/10.15376/biores.12.2.4004-4012>
- Burley J, Evans J, Youngquist J (2004) *Encyclopedia of forest sciences*. Elsevier Academic Press, Oxford

## Publisher's Note

Springer Nature remains neutral with regard to jurisdictional claims in published maps and institutional affiliations.

Submit your manuscript to a SpringerOpen® journal and benefit from:

- Convenient online submission
- Rigorous peer review
- Open access: articles freely available online
- High visibility within the field
- Retaining the copyright to your article

Submit your next manuscript at ► [springeropen.com](https://www.springeropen.com)